Analysis on Hydrofoil Cross-Sections of a Marine Propeller at various radial distances via ANSYS Fluent

Junya Ogawa supervised by Grant Ingram

Abstract—**This report covers the analysis of air flow around 3 hydrofoil cross sections at radial distances $r = 40$, 100 and 170mm from the centre of the hub of a marine propeller, using ANSYS Fluent 23 R2 with mesh discretisation of hydrofoils via POINTWISE 2023, via analysing the effects of the angle of attack α on the fluid flow and behaviour around the hydrofoil such as flow separation and vortices, the drag and lift coefficients, and the viscous and pressure drag at selected Angles of Attack (α) of $\alpha = 0°, 7°$ and $20°$. This is done with its main application in the input of hydrofoil data into ANSYS's Virtual Blade Model (VBM) to greatly simplify the geometry of the propeller and save computational power compared to other methods of modelling marine propellers. Results obtained show stalling C_L values of $0.5787, 0.6231$ and 0.6690, as well as minimum C_D values of $0.05419, 0.03880$ and 0.03881 in order of increasing r, as well as generally increasing level of turbulence as the magnitude of α increased.**

I. INTRODUCTION

THE analysis of underwater thrusters is important within the development of underwater Remotely-Operated Vehicles (ROVs), as underwater thrusters often are compact and allow good manoeuvrability within underwater conditions such as immense pressure compared to at the pressure level at the surface. Thus, a way of shedding light on how such thrusters would work in said conditions would be to conduct simulations using Computational Fluid Dynamics (CFD) programmes such as ANSYS Fluent in this case to investigate the various factors affecting the efficiency of said thrusters, such as the propeller and surrounding geometry.

CFD is a methodology which allows good predictions of fluid flow phenomena across various contexts based on the main mass, momentum and energy conservation laws [cite]. As such, CFD programmes are commonly used within analyses of underwater thrusters as various conditions could be simulated to great accuracy without needing to devote time and material to build a real simulation, which entails building a full working thruster, or portions of in a water tank. Furthermore, CFD models are highly customisable, which enables for analysis flexibility without having to devote many resources to customising models in a real simulation. However, CFD is also known to be quite fickle, in that it contains various sources of error of which simulations can go wrong and as such, a good understanding of the underlying theories is required to build a strong foundation to base the settings of the simulations and interpret said simulation results accurately.

Within ANSYS Fluent, the method which would be used in this project would be hydrofoil analysis. Forces and their associated coefficients acting on said propeller are determined by the geometry of the propeller hydrofoil profile and the flow regime, which will be covered in greater detail in the following sections. Obtaining said data is critical to using VBM, which provides a lower computing alternative to pre-existing methods of analysing propellers. The ANSYS 2023 R2 update gives a new inbuilt user-interface within VBM to which geometrical data of the propeller can be easily inputted for analysis, which may end up saving configuration times via User-Defined Functions (UDFs) which were used prior to the update.

The aim of this project is to tabulate the drag and lift coefficients (C_D and C_L respectively) and their respective angles of attack α for a Reynolds number Re of 10000 with varying Mach numbers Ma at various radial distances r from the hub of the propeller for input within VBM. The phenomena at various angles will also be investigated to gain a better understanding of the propeller performance as a whole, such as analysing the breakdown of drag values at certain angles and the effect of flow separation on different cross-sections at the same angles.

A. Hydrofoil Analysis

To understand the reason behind the selection of the C_L and C_D values for analysis, the topic of lift and drag forces acting on a hydrofoil shape should be better understood.

There are a few theories as to how lift is generated on a body, but in simple terms via Newton's Third Law: As the body deflects an incoming fluid flow, a force is generated to push the air downwards from the foil. Thus, there is an equal and opposite force which acts upwards, which serves as the lift force F_L. However, there exists other more complex theories, such as those based on the lifting line theory which is based on the Kutta-Joukowski circulation theorem and vortex filaments [1]. The drag force F_D is defined as a sum of the various effects of various types of drag forces acting on the body, such as the form and friction drag forces. The form drag is caused by the differential of pressure over the body via the differences in non-inviscid and inviscid flows around said body [2], which causes a backwards facing force on the body [2]. The friction drag is caused by stresses acting on the surface of the body which act tangentially to the surface of said body which also acts backwards on the body [2]. In 2-Dimensions, these forces are summed to give an overall F_D.

The forces F_L and F_D are further defined as follows on the body, where F_L is perpendicular to the hydrofoil chord and F_D parallel to the chord as seen in Figure 1. As such, the forces F_L and F_D can be described via the x and y component forces F_x and F_y respectively as well as α, which is the angle of attack with respect to the chord line:

$$F_L = \cos \alpha \, F_x + \sin \alpha \, F_y \qquad (1)$$
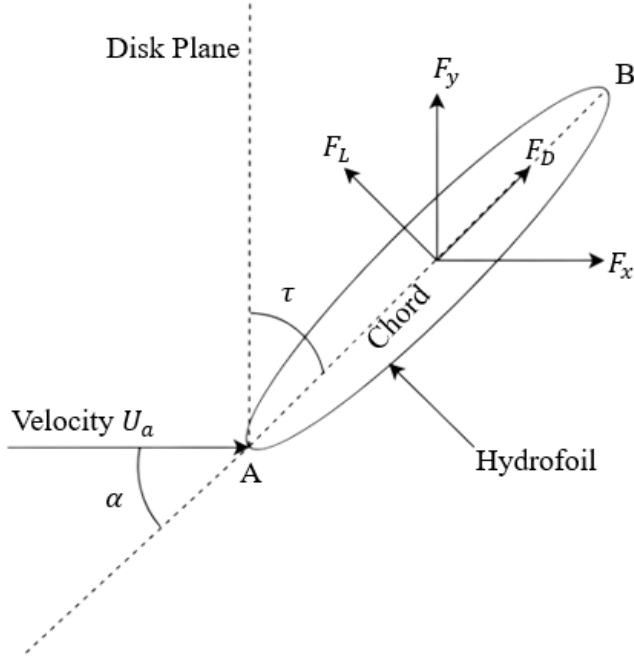$$F_D = -\sin \alpha \, F_x + \cos \alpha \, F_y \qquad (2)$$

Figure 1: *Free body diagram of velocity and force vectors acting on a hydrofoil with chord AB, angle of attack α and propeller twist τ. Note that in this Figure by definition, α is negative and τ is positive.*

As F_L and F_D vary due to numerous factors, a way to quantify them for comparison to other hydrofoils in terms of the local geometry of the body would be to express them in terms of C_L and C_D:

$$C_{L,D} = \frac{F_{L,D}}{0.5\rho U_a^2 A} \qquad (3)$$

Where ρ represents the density of the fluid medium, U_a the fluid velocity which is in contact with the body in question (which can be assumed to be the freestream velocity) and A the reference area. For 2D hydrofoils it can be assumed that A equals c, the length of the chord AB times an arbitrary unit depth with a magnitude of 1.

As α changes, C_L and C_D can be plotted against α. For a typical aerofoil/hydrofoil, as α is increased from 0 to a certain stalling degree α_{stall}, C_L would be expected to linearly proportional to α and C_D to increase gradually [3]. However, it can be expected that C_L would peak to a maximum stalling angle while C_D increases at a larger rate [3]. Thus, the operation of a blade is kept right below α_{stall} to leave some room for adjustment during operation.

B. Blade Element Theory (BET), Blade Element Momentum Theory (BEMT) and the Virtual Blade Model (VBM)

In order to understand how VBM simplifies computational time, an understanding of the fundamental theories behind the model is required. VBM utilises the idea of the BET, which assumes that the forces on a blade can be simplified into two dimensions (with the third dimension ignored): the lift and drag forces [4]. Said forces can be calculated on multiple discretised blade elements via α [4]. From F_L and F_D, integration can be done to obtain the thrust and torque on said blade along the blade length [4]. This is compounded with the implementation of an actuator disk to create momentum source terms to give rise to BEMT, which is more useful as it links the discretisation of forces within the blade to ideas on how to implement the cell topology within mesh generation software such as POINTWISE. To expand on this idea, VBM is the implementation of BEMT in most aspects except for the fact that VBM utilises the Reynolds-Averaged Navier-Stokes (RANS) equations alongside the two 1-dimensional lift and drag equations of BEMT [5] and still uses BEMT data as a basis for simulating the wake flow and the turbulent flow field [5]. Thus, a VBM model would require: 1) The variation of C_D and C_L with respect to α for a set Reynolds number (Re) and Mach number (Ma). 2) The chord length c and α with respect to the ratio of radial distance of cross-section to rotor radius (r/R). 3) Position and orientation angles of the rotor itself [5].

Re is defined as the ratio of inertial and viscous forces acting on a body and is expressed in **Equation 4**:

$$Re = \frac{\rho U d}{\mu} \qquad (4)$$

Where ρ is the fluid density, U the fluid velocity, d the body characteristic length and μ the fluid kinematic viscosity. As Re increases, the greater effect the inertial forces will have on the body and consequently the more turbulence is expected to occur. Generally, flows with $Re > 3500$ are classified as laminar flow. $Re > 3500$ indicates semi-turbulent flow and $Re > 4000$ indicates fully turbulent flow. However, to determine the level of turbulence present more accurately, other variables such as the turbulent kinetic energy will have to be analysed.

In addition, the Mach number Ma is defined as the ratio of the fluid velocity to the speed of sound in the fluid and is expressed as the following:

$$Ma = \frac{U}{a} \qquad (5)$$

Where a is the speed of sound in the fluid. Flows where $Ma < 0.8$ are classified as subsonic, with flows at $Ma > 1.2$ are supersonic and $Ma > 5$ hypersonic. At subsonic flows, the fluid is assumed to be incompressible and so Bernoulli's Principle can be applied. However, at faster speeds fluid is compressible and so other formulae are used. It is expected operating conditions of marine propellers to be subsonic due to the small fluid speeds and its use in VBM only serves as an indication of the medium of which analyses occur in.

Although it can be noted that other simulations may have to be carried out in conjunction with VBM such as the C_L and C_D data, VBM would ultimately help save computational time in the long run, when for example, multiple analyses of the same rotor have to be carried out or when multiple similar rotors are present in the analysed geometry. This would make a

difference especially considering that simulations utilising the BET method often have computation usage magnitudes of times smaller than those utilising full geometries [5], which would indicate faster simulation times in general.

C. Ducted Propeller Thruster System

Ultimately, this analysis plays a part in understanding ducted propeller thruster systems, which necessitates a basic understanding of said systems. Ducted propellers increase the efficiency of marine propulsion systems via axially accelerating the incoming fluid flow which reduces the upstream pressure [6]. This depressurization creates an inwards force which sucks in the fluid [6], as well as decrease any turbulence or pressure fluctuations [7] which improves the thrust generated at zero speed (bollard pull). This is effective at low speeds [8] at which ROVs are known for [9]. Furthermore, to avoid cavitation, thruster propellers have wide blades [7] for large pressure operation. In addition, other factors such as the thrust and torque must be considered in the performance of a thruster system [7], of which the former can be defined by the thruster coefficient C_T. C_T is the ratio of the thrust force to the product of fluid density, the square of revolutions per second and the 4th power of propeller diameter. C_T values tend to be around 0.6 to 0.9 for large thrusters [10] and is dependent on the advance ratio J, which is defined as the ratio of the freestream velocity U_a to the product of the revolutions per second n and the propeller diameter D. If J exceeds its optimal value, then C_T decreases [11]; this can be caused by either the propeller having low rotational speed or a very turbulent incoming flow.

D. VBM and its Modelling Suitability

As the VBM model is mainly used for modelling tidal and wind turbines and its simplification of geometry, there naturally will be concerns regarding the general suitability regarding how well VBM is able to capture the various vortexes and flows around the propeller. Due to the simplified geometry, there will be many differences ranging from wake formations to numerical accuracy compared to simulations which uses the real geometry. The BEMT of which VBM is based on is most useful in determining viscous effects such as the stall or laminar separation at low Re values [12], while at high Re values stall effects are difficult to model without use of turbulence closure models [12]. Thus, by definition, this makes BEMT suitable for simulations involving low advance ratios, which is well within the scope of investigations with optimal thrust coefficient values. Furthermore, as BEMT is a 2-Dimensional Theory, radial forces generated by actual propellers is ignored as only thrust and torque forces are considered in the theory. Thus, Glauert's correction factor can be added into the theory which takes the approximation of a helical wake structure as a series of disk running at velocity from the wake to the free stream [13].

E. ANSYS Fluent and VBM for CFD analyses

1) About ANSYS Fluent

As mentioned in the introduction, CFD analyses are often very time intensive, and as such CFD software such as ANSYS Fluent are computationally powerful pieces of software. Thus, a good understanding of the principles behind its calculations will go a long way into avoiding common mistakes and costing long simulation times, as is commonplace for CFD analyses.

ANSYS Fluent and VBM solves for the RANS equations, which is regarded to be one of the least computationally intensive approaches in computing fluid flows in comparison to other numerical methods such as Large Eddie Simulations (LES) and Direct Numerical Simulations (DNS) [14]. Within the RANS model, there are various turbulence models including the $k - \omega$ Shear Stress Transport (SST) model. This model includes two transport equations: the turbulent kinetic energy (k) and the specific dissipation rate (ω) equations [15], which is stable for low Re. The SST formulation indicates that at the free stream (i.e., close to the solid geometry but away from the boundary layer) the formulation switches over to the more efficient $k - \epsilon$ formulation. However, it should be noted that the $k - \omega$ SST model underpredicts the amount of separation for adverse gradient flows [15].

As for convergence values, the energy normalised residual is to be kept at 1×10^{-6} whilst the remaining normalised residuals is to be kept at 1×10^{-5}, which proves to be sufficient in obtaining the C_L and C_D to a reasonable accuracy. The residuals will be monitored during simulation to ensure they converge properly as well as produce stable and realistic results.

2) VBM within ANSYS Fluent

Within ANSYS Fluent, the current VBM model is based on BEMT. VBM uses two techniques, of which ANSYS tutorials focus on the technique developed by Zori and Rajagopalan that replaces the rotor with a one-cell thick actuator disk with no inflow or outflow boundaries [16]. Although VBM is mainly used for aerodynamical analysis such as helicopter rotors or wind turbines [17] as evidenced by the vast majority of VBM literature about the aforementioned topics, it is found that marine applications (such as sub-sea vehicles) are generally acceptable, given a few constraints [17], such as the surrounding geometry of the disk not being too close to the disk.

II. METHODOLOGY

CAD models of the thruster was provided by an external rover company alongside with other geometry, with the propeller diameter measured 0.390 m and the propeller hub diameter around 0.069m.

A. Obtaining data from the hydrofoil profile

To initiate VBM, data files containing aerodynamic data of the hydrofoil profile must be obtained for loading into ANSYS Fluent. The data is formatted as follows similar to that established in earlier sections (by line): 1) the name of the file. 2) the number of datasets available in said file. 3) either C_L and C_D, which is represented as cd or cl on the file respectively. 4) the Re and 5) the Ma of the dataset, which is followed by 6) α and either one of the coefficients dependent on input of Step 3. Steps 2 to 6 are then repeated for the other coefficient and can be repeated further for different Re and Ma.

In order to proceed with Step 6, a simple 2-dimensional aerofoil simulation would have to be carried out via creating a

C-mesh in POINTWISE and simulating a specified velocity of a certain magnitude at an initial $\alpha = 0$. The process is then recorded on a journal file and repeated for other α from a range of $-20°$ to $20°$. The journal file is then replicated to be repeated for other hydrofoil profiles at $r = 100$mm and 170mm.

B. Creating the 2D C-meshes

1) Mesh quality criteria

To obtain a good accuracy of results, the mesh quality must be good. Firstly, the y boundary thickness value (y) is considered:

$$y+ = \frac{u_\tau y}{v} \qquad (6)$$

Where u_τ represents the frictional velocity, y the boundary cell wall height and v the kinematic viscosity of the adjacent fluid. For the selected $k - \omega$ turbulence model, it is strongly advised that $y+ < 1$ for a good mesh quality. Furthermore, it can be assumed that u_τ equals to the freestream velocity of the incoming flow for simplicity of calculations, especially considering that the matter of analysis is just the flow of air around a hydrofoil section with no other geometry and thus would not necessitate iterations where u_τ is updated.

There also exists other ways to measure the mesh quality beyond the $y+$ value, such as the orthogonal quality and aspect ratio criteria. The former is measured via the angles between the line connecting 2 cell centroids and the normal vectors, and the latter is a measure of how "stretched" a cell is, i.e., how much the cell dimensions deviate from having all its dimensions being of equal length. The orthogonal quality is recommended to be greater than 0.1, whilst the criterion for aspect ratio greatly depends on the geometries of the mesh. However, in general, it is recommended that aspect ratios do not exceed 10 in boundary layer conditions close to the wall boundary layer and not exceed 5 away from the walls.
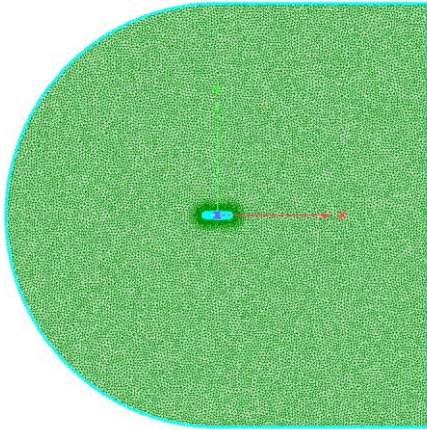
2) Specifications

Figure 2: *C-mesh of a hydrofoil section (r=40mm). The right outermost edge acts as the pressure outlet whilst the remaining outermost edges act as the velocity inlet.*

The propeller was loaded onto SolidWorks and a surface of the cross-section was taken for import into POINTWISE via a surface cut at distances of $r = 40, 100$ and 170mm, which was then followed by first saving the surface cut as an .dwg file, which was then followed via rotating and translating the cross-section such that it was centred at the origin and $\alpha = 0°$.
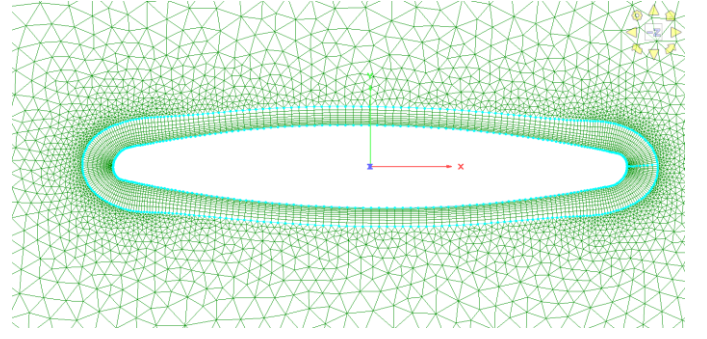

Figure 3: *Close-up of mesh near the boundary layer (hydrofoil of $r = 40mm$)*

Afterwards, the model was traced into 2 parts and a 10-cell thick boundary layer was created with the first cell layer around $y+ < 1$ dependent on the incoming far-stream velocity magnitude with a growth rate of 1.2. The remaining space was then filled in with an unstructured mesh for simplicity, with the height and length of the C-mesh around 10 times the length of the hydrofoil, which was found to be sufficient enough for obtaining an accurate reading of C_L and C_D values.

C. Simulation set-up

After the meshes have been created, they are then exported to ANSYS Fluent 2023 R2 for analysis. The $k - \omega$ SST turbulence model will be employed, with double precision, pressure based, transient Green-Gauss node-based analysis, as well as a transient time of $t = 30$s as this should be enough time for monitored C_D and C_L values to converge sufficiently. This was followed by a maximum of 20 iterations per time step and an implemented coupled scheme with higher order term relaxation. Viscosity ratio is set to 10 for viscous flow with a 5% turbulence intensity, which were the default settings on Fluent. The walls on the hydrofoil cross-sections were set to a no slip condition and no static pressure at the pressure outlet. Air was selected as the fluid medium at 300K. The energy equation was enabled and gravitational effects disabled. Furthermore, as it was found that that only the Re and Ma values had to be accurate to the C_D and C_L values, the choice of fluid medium was not too important as long as the Re and Ma values remained accurate. It was also understood from the ANSYS instruction manual that it would be able to extrapolate the C_L and C_D data for use in the VBM [16], however the extent to which this extrapolation would be accurate is not known.

In order to know what the initial magnitude U_a of the inlet velocity, this number is calculated backwards from a specified $Re = 10000$ for all 3 hydrofoil sections. After some initial calculations, a table of the hydrofoil lengths c and freestream velocity U_a via their distances from the hub and $Re = 10000$ using **Equation 4** for input into each C-mesh:

Table 1: *Hydrofoil lengths at different radial distances and corresponding freestream velocities for analysis.*

	$r = 40$mm	$r = 100$mm	$r = 170$mm
c (mm)	121.28	168.26	140.70
U_a (ms^{-1})	1.2173	0.86141	1.0381

In addition, PRESTO! is selected for the pressure discretisation scheme with no pseudo-time effect as result convergence will be expected to occur relatively quickly.

Now that the initial conditions have been covered, the Cases of this report will be covered. There are three main cases considered by this project. The first of these is Case 1, where the hydrofoil section at the distance $r = 40$mm will be analysed via its C mesh. This is then followed by Cases 2 and 3, which are the analyses of the flow around the $r = 100$mm and the $r = 170$mm hydrofoil section respectively. Results such as the velocity profiles, the turbulent kinetic energies and the drag coefficient breakdown at selected α will be chosen, which would then be followed by an analysis of the trend of C_L and C_D values from all 3 Cases with respect to α.

III. RESULTS

A. Overview

In total, there were a total of 41 simulations ran for the data for each α value across each hydrofoil, which meant a total of 123 simulations run for this project. However, in the following analyses, only 9 simulations will be taken for consideration: for the angles $\alpha = 0°, 7°$ and $20°$ at each Case. Each simulation averaged around 40 minutes in run time dependent on how fast they converged (for larger α, simulations required more iterations), which meant that an estimated 82 hours of computational time was used across the 123 simulations. The number of iterations required for each α value ranged from around 6000 to 30000 across the 3 Cases, dependent on how well they converged. Each simulation was run on 4 processes, taking around 20MB of memory.

Via the length of the hydrofoil profiles and with a $Re = 10000$, the Mach numbers Ma for each profile was calculated respectively using **Equation 5**. The value of a was taken to be $341 \; ms^{-1}$ at 300K and atmospheric conditions, which were the chosen conditions for the report. These results were then tabulated with the number of cells of each hydrofoil C-mesh, the minimum orthogonal quality, and the maximum aspect ratio, which shows that the C-meshes in all 3 Cases are of sufficient quality alongside the consideration of the $y+$ values as stated in **Table 2**.

Table 2: *Table of various mesh quality data alongside the Mach Number and percentage thickness.*

Distance r (mm)	40 (Case 1)	100 (Case 2)	170 (Case 3)
Total Number of Cells	39120	39520	39780
Minimum orthogonal quality	0.4924	0.5013	0.4960
Maximum aspect ratio	5.742	5.543	5.516
Mach Number Ma	0.003602	0.002547	0.003064
Thickness (%)	16.1%	6.99%	3.38%

In addition to this, a good transient time step Δt required for convergence was found to be $\Delta t = 0.01$s, as a lower Δt values would mean greater accuracy at the end of the simulation yet require a longer computational time, which was not too feasible given the timespan of the project. On the other hand, a higher Δt value meant that the monitored C_D and C_L values were not able to converge properly at high α due to the instability at relatively higher values of Δt such as tested values of $\Delta t = 1$s.

As the propeller was meant to be run in reverse as well as checking the geometry of each hydrofoil, it was found that the dimensions of the cross-sections were mirrored and reversed across the x-axis such that the C_D and C_L at $\alpha = \pm180°$ equaled that at $\alpha = 0$. Therefore, there was no need to calculate values at $\alpha = \pm180°$ to complete the data files. Furthermore, upon running the simulations, it was found that values were converging before $t = 20$s in general (i.e., when the energy residuals were below 1×10^{-6} and the other residuals below 1×10^{-5}), but in certain α values, it took a slightly longer transient time to converge. This could be due to the flow separation occurring at a certain α which made the flow more unsteady and thus take longer to converge.

1) Convergence of monitored C_D and C_L

On the topic of convergence of the C_D and C_L coefficients, it was found that that in most cases, the coefficients converged to the 7th decimal place, however, there existed some cases where it was not converging to that extent so an average of the readings from $t = 25$s to $t = 30$s were taken. However, it should be noted that within example tutorial files made by ANSYS, results were used up to the 4th decimal place so accuracy of said results would have been more than sufficient for VBM usage.

To further analyse the convergence of results, the net mass imbalance of each mesh was plotted on a contour at selected values of $\alpha = 0°, 7°$ and $20°$ at a transient time $t = 30$s to calculate the difference of the mass inflow and outflow of each cell: a smaller value is better for convergence as it means the results is closer to adhering to the principle of conservation of mass within CFD, i.e., that there is no net change between the mass inflow and mass outflow in a control volume of a cell. It was found that at $\alpha = 0°$, magnitude of the maximum mass imbalances was found to be at 1.86×10^{-12} kg s^{-1} at $r = 40$mm, with larger mass imbalances values concentrated near the boundary layer of the hydrofoils in all 3 cases. Similarly, at $\alpha = 7°$ the maximum mass imbalance was found to be at from 1.64×10^{-15} kg s^{-1} and for $\alpha = 20°$ this maximum mass imbalance was 1.84×10^{-12} kg s^{-1}.

By looking at the overall magnitude of the mass imbalance, it was found that the results were adequately converged as there was a negligible difference between the mass flow into a cell and out of the cell which further validates the results of this project.

B. Fluid Flow characteristics at varying α and r values

Velocity and turbulent kinetic energy contours were created from the 9 simulations with the intent to better understand the flow of fluid around them and any turbulent flow properties that may arise from different α.
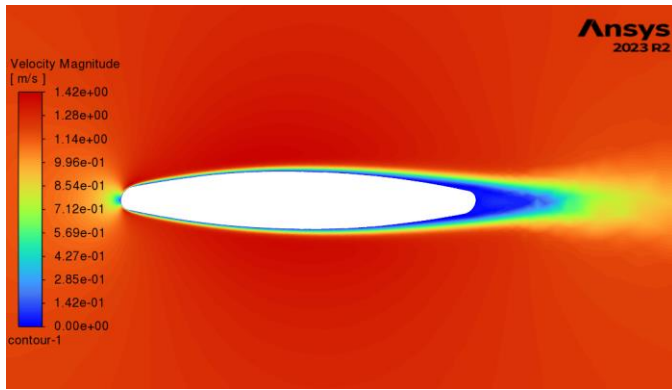
1) Case 1: $r = 40mm$ hydrofoil

Figure 4: *Velocity contour at $r = 40mm$, $\alpha = 0°$*

It can be seen from **Figure 4** that at $\alpha = 0°$, there is a rather straightforward flow of air around the hydrofoil: air meets the front edge of the hydrofoil at a normal and this results in a divergence of flow along the upper and lower edges. The air velocity can also be observed to decrease as it gets closer to the edges and is at 0 when it meets the wall surface: this is due to the no-slip condition of the wall boundary, which states that there is a zero-bulk velocity at the boundary layer of the wall.

Moving along longitudinally, the flow of fluid roughly conforms to the hydrofoil as the hydrofoil shape flattens out, which is due to the Coanda effect. This means that the incoming fluid flow tends to attach to the convex surface of the hydrofoil. Towards the trailing edge, the flow separation between the hydrofoil and air gets larger at the edges of the hydrofoil. It could be noted that the flow separation at the trailing edge is more significant to other hydrofoil shapes; this could be due to the bluntness of the trailing edge (as the hydrofoil is meant to operate in reverse, the trailing edge would be equally as "blunt" as the leading edge due to the symmetric geometry) which meant the two flows above and below the hydrofoils converged behind the trailing edge. However, there still appeared to be some turbulence after the convergence of the two air streams where the border of the wake appears to diverge and the air dissipates. This could be due to the blunt geometry of the hydrofoil, where the crossing of the air flows at such an angle made by the hydrofoil created some turbulence in addition to the high Re of 10000. However, flow still appears to be mostly steady from the leading to trailing edge.

At $\alpha = 7°$, the flow now meets the hydrofoil at an angle as seen in **Figure 5**. This results in the flow separation on the upper edge occurring further away from the trailing edge and the flow separation on the lower edge closer to the trailing edge. Compared to at $\alpha = 0°$, the maximum velocity is now observed to be at 1.87 ms^{-1} instead of 1.42 ms^{-1}. This indicates a better performance at $\alpha = 7°$ as the propeller spins faster which generates more thrust compared to $\alpha = 0°$, although it should be noted that the area of high velocity is more concentrated near the front upper edge of the hydrofoil, instead of the more consistent fluid flow at $\alpha = 0°$. After the small initial separation, it should be noted that the flow briefly re-attaches itself back to the surface as seen previously despite the small vortex, which is again another observation of the
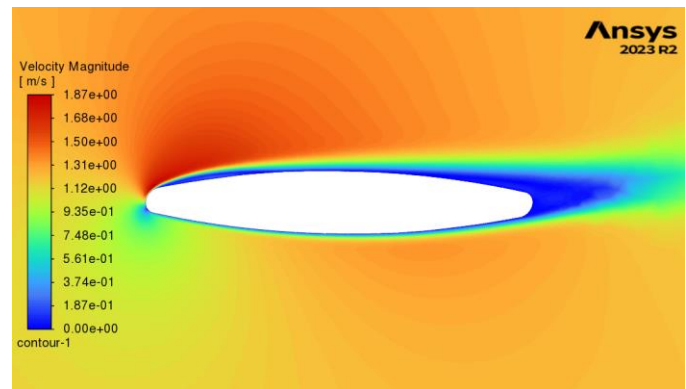

Figure 5: *Velocity contour at $r = 40mm$, $\alpha = 7°$*

Coanda effect. In addition, it could be noted that the bottom edge of the hydrofoil experienced the Coanda effect throughout the length of the hydrofoil where the flow attached to the surface until the trailing edge. This had made the flow below the hydrofoil less unsteady than at the top, but still similar to observations made at $\alpha = 0°$. However, it could be noted that after the 2 airstreams meet after the trailing edge, it appears that the resulting wake is less turbulent than the flow observed at $\alpha = 0°$, where the angle formed between the converging 2 airstreams is smaller.
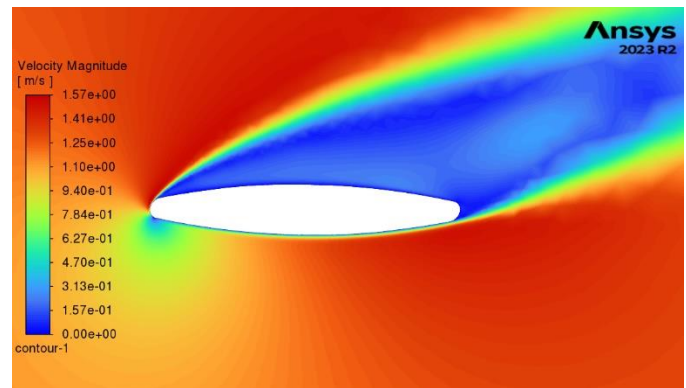

Figure 6: *Velocity contour at $r = 40mm$, $\alpha = 20°$. Wake was not fully captured in this Figure as it extended to the boundaries of the C-mesh.*

Lastly, at $\alpha = 20°$, the angle of coincidence of air is high enough that flow separation occurs above the upper edge next to the leading edge instead of near the trailing edge as seen in **Figure 6**. This large flow separation results in unsteady vortices above the upper edge which proves operation at this angle inefficient as a significant amount of kinetic energy provided by the incoming air flow will be lost to said vortices, despite the maximum velocity of 1.57 ms^{-1} is shown to be greater than that at $\alpha = 0°$, thus the hydrofoil operation at this angle will produce less thrust. This also shows a quick transitioning to turbulent flow above the upper edge right after the brief flow attachment to the leading edge due to the vortices formed right above the hydrofoil. Like previous observations, it should be noted that the flow at the lower edge now is attached to most of the lower edge of the hydrofoil, but it also quickly diverges to a turbulent flow at a smaller distance than previous examples with lower α.

To further visualise this point, the maximum turbulent kinetic energy at the area of flow separation is around 1.20×10^{-1} m²s², compared to values of 3.44×10^{-2} m²s² at $\alpha = 0°$ and 4.55×10^{-2} m²s² at $\alpha = 7°$, which indicates on average more kinetic energy was lost to turbulence at $\alpha = 20°$ and thus the least kinetic energy was available for operating the hydrofoil at $\alpha = 20°$ compared to the other two α values. It should also be noted that at $\alpha = 0°$, the concentration of turbulent kinetic energy loss occurred in between the convergence of the upper and lower air flows and the wake rather than in $\alpha = 7°$, where there was some turbulent kinetic energy lost near the leading edge or at $\alpha = 20°$, where most of the losses were in the wake.

Table 3: *Case 1 form and friction C_D breakdown*

$r = 40mm$	$\alpha = 0°$	$\alpha = 7°$	$\alpha = 20°$
Friction C_D (proportion)	0.02676 (49.37%)	0.01881 (26.22%)	0.01947 (6.50%)
Form C_D (proportion)	0.02744 (50.63%)	0.05293 (73.78%)	0.2802 (93.50%)
Total C_D	0.05419	0.07174	0.2997

Next, the breakdown of the C_D into its friction and form components was done to analyse the level of flow separation present in the hydrofoil via using a post-processing forces report, as tabulated in **Table 3**. It can be seen that the form C_D generally increased as α increased; this is due to the fact that at higher α, there was more flow separation which resulted in a higher pressure-differential between the inviscid and boundary layer flows. The form C_D also compromised a majority of the proportion of the total C_D in all 3 α values.

2) Case 2: $r = 100mm$ hydrofoil

Next, the velocity and turbulent kinetic energy values for the hydrofoil profile at $r = 100mm$ were monitored at the same α of $0°, 7°$ and $20°$ at $t = 30s$ when monitored C_D and C_L values were found to be sufficiently converged. It was found that at $\alpha = 0°$, velocities reached a high of 9.96×10^{-1} ms^{-1} and with a maximum turbulent kinetic energy of 2.78×10^{-3}. At $\alpha = 7°$, these were at 1.18 ms^{-1} and 4.30×10^{-2} m²s² respectively and at $\alpha = 20°$, these were 1.08 ms^{-1} and 6.90×10^{-2} m²s². It can be observed that the overall trend of the velocities and the turbulent kinetic energies were consistent with that found in the previous sub-section: maximum velocities peaked at $\alpha = 7°$ with the maximum velocity at $\alpha = 0°$ being the lowest and the maximum velocity at $\alpha = 20°$ in between these two values. As for the turbulent kinetic energies, there was an increase in turbulent kinetic energy when α increased due to the increased flow separation.

It should also be noted that at $\alpha = 7°$, there was a greater amount of flow separation towards the leading edge rather than towards the trailing edge for Case 1 as can be seen in **Figure 7** where the turbulent kinetic energy contour extends for nearly the whole length of the hydrofoil; this could be due to the more streamlined shape of the hydrofoil stemming from the smaller thickness (6.99% compared to Case 1's 16.1%) which allowed vortices to form closer to the leading edge compared to Case 1.

In general, the turbulent kinetic energies were lower than that of their counterparts at r = 40mm. Due to the same Re, it
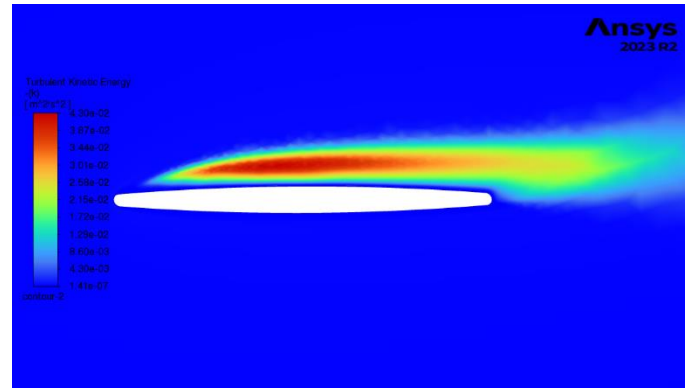

Figure 7: *Turbulent Kinetic Energy contour at $r = 100mm$, $\alpha = 7°$.*

could be determined that this was due to the geometric properties of the hydrofoil. As mentioned earlier, the hydrofoil was more streamlined than its counterpart at $r = 40mm$, less energy was wasted to the formation of vortices and more energy was put into powering the propeller.

Table 4: *Case 2 form and friction C_D breakdown*

$r = 100mm$	$\alpha = 0°$	$\alpha = 7°$	$\alpha = 20°$
Friction C_D (proportion)	0.02618 (67.48%)	0.01215 (13.88%)	0.01779 (5.83%)
Form C_D (proportion)	0.01262 (32.52%)	0.075387 (86.12%)	0.2875 (94.17%)
Total C_D	0.03880	0.08754	0.3053

Looking at the form and friction C_D breakdown, it can be noted that the general trend of the form C_D increased as α increased. However, there are a few notable differences compared to that examined at Case 1: at $\alpha = 0°$ the friction C_D now constitutes the majority proportion instead of the form C_D. This could be due to the thinner hydrofoil in Case 2: the percentage thickness of 6.99% compared to the 16.1% at Case 1 meant that in Case 2, there was a much smaller pressure differential which added with its much smaller relative thickness made for a smaller contribution (which caused less divergence of the upper and lower flows) of form C_D to the total drag.

Furthermore, it can be observed that the form C_D proportion is higher than that in their Case 1 counterparts: this would be due to the higher levels of form separation as observed earlier from the turbulent kinetic energy plot.
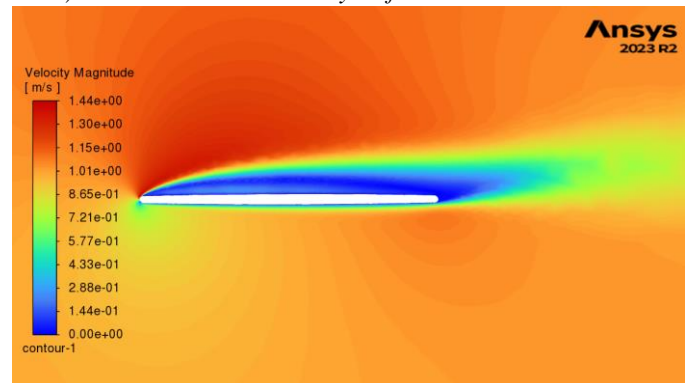
3) Case 3: $r = 170mm$ hydrofoil

Figure 8: *Velocity contour for $r = 170mm$, $\alpha = 7°$*

Following this, the same process was repeated for the same α at the distance r = 170mm. It was found that in increasing

order of α, the maximum velocities were $1.23, 1.44$ and $1.33 \ ms^{-1}$. For the maximum turbulent kinetic energies, these were $3.07, 5.96$ and $9.91 \times 10^{-2} m^2 s^2$. It can be noted that in comparison to values in Subsection A.1 and A.2, there was a greater net turbulent kinetic energy and velocities across the same α. Flow separation still occurred at $\alpha = 7°$ with no reattachment of the flow back to the hydrofoil surface just like in Case 2 but with the recirculatory vortex spanning a longer length of the hydrofoil and with fully turbulent flow of air above the upper edge at $\alpha = 20°$.

Table 5: *Case 3 form and friction Cd breakdown*

$r = 170$mm	$\alpha = 0°$	$\alpha = 7°$	$\alpha = 20°$
Friction C_D (proportion)	0.02966 (76.43%)	0.01264 (13.22%)	0.01790 (5.69%)
Form C_D (proportion)	0.009145 (23.57%)	0.082950 (86.78%)	0.29655 (94.31%)
Total C_D	0.03881	0.09559	0.3145

The breakdown of drag also followed trends largely set in Case 2: an initial large friction C_D at $\alpha = 0°$ but with the form C_D taking the majority of the C_D breakdown at larger α. The form C_D at $\alpha = 0°$ is noted to be now smaller than its counterpart in Case 2 due to the smaller thickness of 3.38% compared to Case 2's thickness of 6.99%, which also resulted in larger flow separation than Case 2 as evidenced by the larger form at C_D proportions at larger at α.
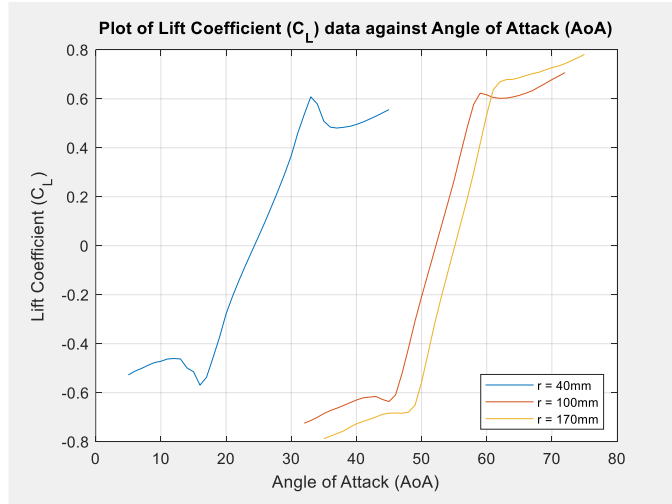
C. Analysis of C_L values

Figure 9: *Graph of C_L vs. α with α adjusted for twist τ*

To follow up, a graph of C_L was plotted against α as shown in Figure Cd. Due to the decreasing twist τ as r increased, this meant that by definition, the median value of α (noted as α_0) of each hydrofoil increased as r increased, as seen by $\alpha_0 = 25°, 52°$ and $\alpha_0 = 55°$ in increasing order of r. It can also be seen from these values that the twist is not linearly proportional to α_0; instead near the tip, the twist τ decreased at a smaller rate than that closer to the hub, which made the blades flatten out at the tip and therefore proved consistent to observations made about the CAD design of the propeller.

The C_L values at the specified distances were also plotted similarly to that in the previous sub-section. At their respective α_{stall} (i.e., where there was a peak in the C_L value),

the C_L at $r = 40$mm was the lowest at 0.57874 at $\alpha_{stall} = 34°$, which was followed by $C_L = 0.62311$ at $\alpha_{stall} = 59°$. It was not so clear where the stalling angle was for $r = 170$mm as the magnitude of C_L was strictly increasing as α increased from $\alpha_0 = 55°$, thus making it difficult to establish a clear peak. This is due to the thickness of the hydrofoil shapes; the hydrofoil cross-section closest to the hub is the thickest to give the propeller strength as well as the smaller rotational velocity acting near the hub compared to the tip. As the hub distance increased the thickness decreased due to the higher rotational velocity which resulted in the flattening of the peak, which made it harder to determine the peak C_L at higher values of r. However, if the value at the end of the linear section of the graph was taken, then the α_{stall} in Case 3 would have been at $62°$ with a C_L of 0.6690. In regard to the maximum values of C_L, it was found that at the upper boundaries of the α range in increasing values of r, C_L was at 0.2997, 0.3053 and 0.3145.

It also can be noted that the trends of the graph correspond roughly to theory: at small magnitudes of α close to the median α_0, C_L was somewhat linearly proportional to α. This was more apparent in the Case 2 and 3 hydrofoils where this linear range was larger compared to the Case 1 hydrofoil where the range was smaller.

This was not to say that were no stalling effects evident throughout the range of α for $r = 170$mm due to the lack of decrease of C_L after the peak C_L value (which is usually the case); there exists the flow separation as mentioned in **Section B** as well as the sharp increase in the C_D which will cause the hydrofoil to stall. However, around the optimal angle the C_L lot at $r = 170$mm was generally around that of counterparts of lower distances; at increasing levels of r they were found to be at 0.5364, 0.4822 and 0.5354.
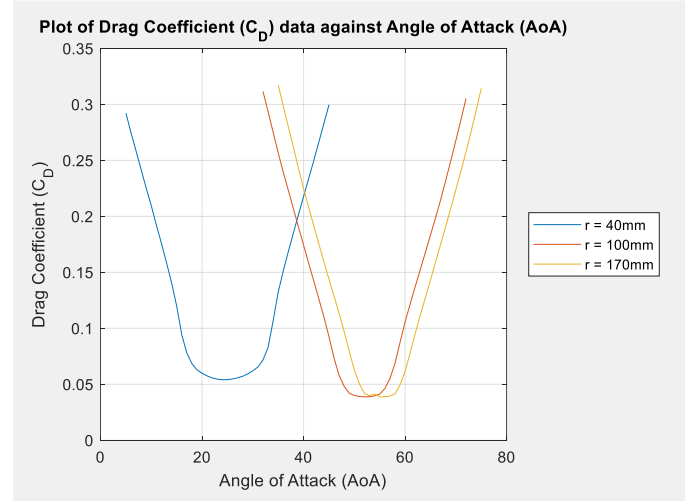
D. Analysis of C_D values

Figure 10: *Graph of C_D vs. α with α adjusted for twist τ.*

The C_D values were plotted similarly to the previous subsection. It can be seen from the Figure that closer to the hub at $r = 40$mm, there was a smaller minimum C_D (C_{Dmin}) compared to the other C_D values at $r = 100$ and 170mm near their respective α_0 values, with $C_{Dmin} = 0.05419, 0.03880$ and 0.03881 in increasing r. As the α magnitude increased, C_D increased slowly until the Cases' respective α_{stall} had been

met; in which case C_D increased much faster in an approximately linear fashion across the 3 hydrofoils (which was due to the presence of flow separation and much more turbulent flow) until the maximum C_D values (C_{Dmax}) across all of them were at $0.29227, 0.31164$ and 0.31727 in order of increasing distances. This is also roughly consistent with expected trends from literature, which predicts a roughly initial constant C_D near α_0 and with C_D linearly increasing as α increased. It could also be noted that in both Cases 2 and 3, obtained C_D plots are quite similar with near identical C_{Dmin} and gradient of linear increase: this is due to their very similar geometrical properties.

E. Summary of results

The effect of α on the values of C_L are dependent on the geometry of the hydrofoil and the far-stream speed of air given the same Re across the 3 Cases but was generally found to have a linear relationship before peaking at an optimum stalling angle with associated C_{Lstall} as tabulated below. As for the C_D values, they were found to have a minimum C_{Dmin} before increasing in an approximately linear manner:

Table 6: *Table of collected α_{stall}, corresponding C_{Lstall} as well as C_{Dmin}.*

	Case 1	Case 2	Case 3
C_{Lstall}	0.57874	0.62311	0.6690
α_{stall} (with respect to α_0)	34° (9°)	59° (7°)	62° (7°)
C_{Dmin}	0.05419	0.03880	0.03881

IV. EVALUATION

This report provides valuable insight into the operation of hydrofoils at different α, yet there remain more to be improved to the level of analysis. For example, the fluid medium of this report is air, yet hydrofoils mainly operate in water. Furthermore, the Re of said report remained at a fixed 10000 despite operations of said thruster of which the hydrofoils belong to is more to the scale of 100000. Even through the turbulent threshold has been passed and as such the C_L and C_D trends will be very similar and have similar values as mentioned earlier, the only notable exception to this would be the α_{stall} would be smaller as flow separation would occur at a smaller α due to the increased Re. The improved Re and fluid medium is just to make results in VBM more accurate and can also be used in conjunction with lift and drag data obtained in this report via formatting the data files.

In addition, there are also more efficient ways of conducting this report. For example, the C_L and C_D data could have been collected using XFOIL, which mainly analyses pressure distributions on sub-sonic aerofoils and requires the coordinates of points on said aerofoils. The analysis of the turbulent characteristics at the specified α could have been carried our separately, meaning only around 12 simulations would have been carried out in total (including the pressure simulations of the 3 Cases on XFOIL). This would have saved tens of hours on running journal files on ANSYS Fluent.

The scope of the project was also limited by the range of α, where in all 3 Cases it was limited to between $-20°$ and $20°$.

By extending the range of α, further phenomena such as the formation of Von Karman vortexes caused by vortex shedding at the high α and consequently, hydrofoil oscillations and the Strouhal number can be analysed to gain further insight of the hydrofoil. This also has the additional advantage of making VBM analyses more accurate due to the larger number of data points.

Furthermore, there is not really any data to compare the C_L and C_D to as this thruster has never undergone through this type of hydrofoil analysis: the best that can be done is to compare this data and its trends to similar hydrofoils at similar Re, analysing the residuals from simulations or conducting water tank tests of the hydrofoil section.

V. CONCLUSION

The effect of varying α on the velocity and turbulence levels are generally summed up as follows: the greater the α, the greater the turbulence, yet velocities hit a maximum at $\alpha = 7°$ independent of hydrofoil shape, which indicated an optimum operating angle of which the hydrofoil operates at. C_L and C_D trends with respect to α generally followed trends established in literature, with peak C_{Lstall} of $0.5787, 0.6231$ and 0.6690 and minimum C_{Dmin} of $0.05419, 0.03880$ and 0.03881 in increasing order of r. Coanda effect was observed at all values of α: at the upper edge this effect was reduced when α increased, but on the lower edge this effect was increased when α increased and caused steady flow until the trailing edge. Turbulent flow was observed on all 9 simulations in this report near the boundary layer, but flow separation occurred notably at $\alpha = 7°$ and $20°$ in all Cases.

VI. ACKNOWLEDGEMENTS

VII. BIBLIOGRAPHY

[1]   H. Jacobson, 'Simulations of a self-stabilizing fully submerged hydrofoil', KTH Royal Institute for Technology, Stockholm, 2023.

[2]   E. L. Houghton, P. W. Carpenter, S. H. Collicott, and D. T. Valentine, 'Basic Concepts and Definitions', in *Aerodynamics for Engineering Students*, Elsevier, 2017, pp. 1–86. doi: 10.1016/B978-0-08-100194-3.00001-8.

[3]   S. Worasinchai, 'Small Wind Turbine Starting Behaviour', University of Durham, Durham, 2012. [Online]. Available: http://etheses.dur.ac.uk/4436/

[4]   H. Hou, W. Shi, Y. Xu, and Y. Song, 'Actuator disk theory and blade element momentum theory for the

force-driven turbine', *Ocean Engineering*, vol. 285, p. 115488, Oct. 2023, doi: 10.1016/J.OCEANENG.2023.115488.

[5]   S. Radfar, B. Kianoush, M. Majidi Nezhad, and M. Neshat, 'Developing an Extended Virtual Blade Model for Efficient Numerical Modeling of Wind and Tidal Farms', *Sustainability*, vol. 14, no. 21, p. 13886, Oct. 2022, doi: 10.3390/su142113886.

[6]   M. Remaud, P. M. Guilcher, J. B. Leroux, and Laurens J. M., 'Design of ducted propellers', Lisbon.

[7]   K. Keillor, 'Analysis of Interaction Effects for a Remotely Operated Vehicle Thruster using Computational Fluid Dynamics', University of Durham, Durham, 2023.

[8]   Fahri Celik, Ali Dogrul, and Yasemin Arikan, 'Investigation of the Optimum Duct Geometry for A Passenger Ferry', May 2011.

[9]   P. Aird, 'Deepwater: Essentials and Differences', in *Deepwater Drilling*, Elsevier, 2019, pp. 165–224. doi: 10.1016/B978-0-08-102282-5.00005-3.

[10]   J. Liu, Q. Yue, C. Zeng, and Y. Zhang, 'Numerical Analysis of the Thrust Characteristics of Propulsion Systems of Hybrid Remotely Operated Vehicle', *Iranian Journal of Science and Technology, Transactions of Mechanical Engineering*, Jul. 2023, doi: 10.1007/s40997-023-00689-z.

[11]   A. Brezina and S. Thomas, 'Measurement of Static and Dynamic Performance Characteristics of Electric Propulsion Systems', in *51st AIAA Aerospace Sciences Meeting including the New Horizons Forum and Aerospace Exposition*, Reston, Virigina: American Institute of Aeronautics and Astronautics, Jan. 2013. doi: 10.2514/6.2013-500.

[12]   A. B. Phillips, S. R. Turnock, and M. Furlong, 'Evaluation of manoeuvring coefficients of a self-propelled ship using a blade element momentum propeller model coupled to a Reynolds averaged Navier Stokes flow solver', *Ocean Engineering*, vol. 36, no. 15–16, pp. 1217–1225, Nov. 2009, doi: 10.1016/j.oceaneng.2009.07.019.

[13]   S. A. El-Shahat, G. Li, F. Lai, and L. Fu, 'Investigation of parameters affecting horizontal axis tidal current turbines modeling by blade element momentum theory', *Ocean Engineering*, vol. 202, p. 107176, Apr. 2020, doi: 10.1016/j.oceaneng.2020.107176.

[14]   A. F. Molland and S. R. Turnock, 'Theoretical and numerical methods', in *Marine Rudders and Control Surfaces*, Elsevier, 2007, pp. 233–311. doi: 10.1016/B978-075066944-3/50009-3.

[15]   F. Menter, 'Zonal Two Equation k-w Turbulence Models For Aerodynamic Flows', in *23rd Fluid Dynamics, Plasmadynamics, and Lasers Conference*, Reston, Virigina: American Institute of Aeronautics and Astronautics, Jul. 1993. doi: 10.2514/6.1993-2906.

[16]   L. A. J. Zori and R. G. Rajagopalan, 'Navier—Stokes Calculations of Rotor—Airframe Interaction in Forward Flight', *Journal of the American Helicopter Society*, vol. 40, no. 2, pp. 57–67, Apr. 1995, doi: 10.4050/JAHS.40.57.

[17]   ANSYS Inc., *ANSYS Fluent User's Guide*. Canonsburg, PA: ANSYS Inc., 2023.